X-ray microtomography analysis of the damage micromechanisms in 3D woven composites under low-velocity impact

R. Seltzer [a], C. González [a,b], R. Muñoz [a], J. LLorca [a,b,*], T. Blanco-Varela [c]

ABSTRACT

3D woven composites reinforced with either S2 glass, carbon or a hybrid combination of both and containing either polyethylene or carbon z-yarns were tested under low-velocity impact. Different impact energies (in the range of 21–316 J) were used and the mechanical response (in terms of the impact strength and energy dissipated) was compared with that measured in high-performance, albeit standard, 2D laminates. It was found that the impact strength in both 2D and 3D materials was mainly dependent on the in-plane fiber fracture. Conversely, the energy absorption capability was primarily influenced by the presence of z-yarns, having the 3D composites dissipated over twice the energy than the 2D laminates, irrespective of their individual characteristics (fiber type, compaction degree, porosity, etc.). X-ray microtomography revealed that this improvement was due to the z-yarns, which delayed delamination and maintained the structural integrity of the laminate, promoting energy dissipation by tow splitting, intensive fiber breakage under the tup and formation of a plug by out-of-plane shear.

1. Introduction

Standard composite materials are manufactured by stacking plies containing either unidirectional or bidirectional fiber tows or fabrics. This approach is ideal to maximize the in-plane composite properties as the fibers, which provide stiffness and strength, are oriented within the plane but the out-of-plane properties of these 2D laminates are limited. This is particularly critical under out-of-plane impact because interply decohesion may develop even in the absence of visible damage in the top and bottom plies [1]. These delaminations lead to major reductions in the compressive strength because the laminate is subdivided into thinner sublaminates with lower buckling load.

One successful strategy to improve the out-of-plane mechanical properties of the 2D laminates has been the development of 3D fabrics by binding 2D preforms in the out-of-plane direction using either z-pinning, stitching or weaving. In particular, woven orthogonal preforms have gained rapid impulse, since traditional 2D weaving machines could be adapted to build these 3D fabrics. Furthermore, the resulting composites made by polymer infusion of the 3D fabrics (hereafter called 3D composites) have shown outstanding mechanical properties in terms of damage tolerance [2,3], delamination resistance, notch sensitivity [2], and energy absorption during out-of-plane impact [4] as compared with the 2D counterparts.

Obviously, the presence of reinforcements in the out-of-plane direction leads to more complex deformation and damage micromechanisms. This information is critical to optimize the mechanical performance as well as to develop accurate models to simulate the mechanical performance of 3D composites [5,6] and has been addressed in various investigations. For instance, Walter et al. [7] studied the effect of strain rate in the out-of-plane behavior of 3D glass fiber composites using optical microscopy. They observed that z-yarns prevented delamination at low strain rates and low penetration depths, and the main damage mechanisms under these conditions were intratow and resin pockets cracking as well as fiber failure. However, delamination damage – as in 2D composites – also occurred at high strain rates or high penetration depths. Baucom and Zikry [8,9] explored the behavior under impact of glass fiber 2D and 3D composites with optical and scanning electron microscopy, which allowed a better insight of the damage micromechanisms. They concluded that the larger energy absorption of the 3D composites was due to the following mechanisms activated by the z-yarns: extensive straining of the z-yarns, z-yarn fracture and surface weft tows pulled through unbroken crimp of the z-yarns. The authors suggested that the perforation resistance and overall behavior of 3D composite systems could be tailored by modifying the mechanical properties of the z-yarns.

One shortcoming of these previous investigations was the use of 2D damage characterization techniques (visual inspection, optical or scanning electron microscopy, ultrasound) to ascertain damage processes that are inherently 3D because of the architecture of the composite. This limitation can be overcome with the use of X-ray computed tomography (XCT), which can provide 3D information of the damage mechanisms with high resolution without alteration of the specimen. The application of XCT to characterize processing defects and damage micromechanisms in 2D composites is relatively new [10–14] and it has demonstrated its potential to ascertain the beneficial effect of glass fiber hybridization on the energy absorption capability of the 2D woven carbon fiber/epoxy laminates [15]. Moreover, XCT was recently applied to 3D composites [16,17] and, in particular, Gerlach et al. [17] used a combination of optical 3D microscopy, ultrasound and low resolution XCT to find out the influence of the z-yarn volume fraction in the delamination resistance.

Following this direction, the present work intends to elucidate the role of the 3D architecture in the out-of-plane low-velocity impact resistance and the corresponding failure micromechanisms. Rather than study damage initiation (a critical issue in 2D composites which are prone to delamination), this investigation was aimed at determining the factors controlling the maximum load supported by the laminate and the total energy dissipated which depend not only on the mechanisms of damage initiation but also on the propagation of damage through the layered structure. Penetration resistance and energy dissipated were determined from the load–displacement curves, which were analyzed to the light of the damage processes characterized by means of ultrasound and XCT. The performance of the 3D composites was compared with the impact response of 2D laminates composed of multidirectional woven plies. This comparison was carried out on the basis that woven fabric prepregs with multidirectional stacking sequence present the best out-of-plane strength and toughness from all 2D architectures [18,19].

Having in mind the difficulties to replace 2D laminates by 3D composites in many applications (porosity, compaction degree, limitations to vary their thickness, lower conformability, low supply), we would like to answer the question in which situations 3D composites out-perform the traditional 2D laminates.

2. Materials and experimental techniques

2.1. Materials

3D composites manufactured by vacuum infusion of an epoxy vinylester resin in three different 3D orthogonal woven preforms were studied in this investigation. The commercial name of the materials, their manufacturer, nomenclature, matrix, fiber and fabric characteristics as well as the composite thickness and areal density can be found in Tables 1 and 2. The 3D composites were made up by alternating layers formed by fiber tows oriented in the warp and weft direction. The 3D_S2 composite had nine warp and weft layers while the 3D_hyb composite had 2.5 consecutive warp and weft layers made from carbon fiber, followed by 4.5 consecutive warp and weft layers made from S2 glass fiber (Fig. 1). In both cases, the z-yarn binder was made up of ultra-high molecular weight polyethylene (PE) fiber (Dyneema). The 3D_C composite had seven carbon fiber warp and weft layers and its binder was also made from carbon fiber. It should be noticed that the lay-up of the hybrid 3D composite was not symmetric and these specimens were impacted with the glass fibers in the backside (non-impacted) surface (Fig. 1).

In addition to the 3D composites, a 2D multidirectional woven material was also studied to compare their response against out-of-plane impact. The 2D_S2 composite was manufactured by hot pressing a stack of pre-preg sheets made up of S2 glass fibers with 8-harness satin structure embedded in an epoxy resin. The stacking sequence was $[(\pm45/0/90)_2/0]_s$. Curing was carried out at 2 bars of pressure and the temperature was raised at 2 °C/min up to 130 °C and held for 2 h; afterwards, the temperature was raised at 2 °C/min up to 180 °C and held for another 2 h. Cooling up to room temperature was performed at 8 °C/min and the pressure was released after 20 min.

2.2. Low-velocity impact tests

Low-velocity impact tests were carried out using an Instron Dynatup 8250 drop weight testing machine. Square specimens of 145×145 mm^2 were cut from the composite panels. The composite plates were simply supported by the fixture and hold at the corners with special clamping tweezers, leading to a free impact area of 127×127 mm^2 (Fig. 2). The specimens were impacted at the center using a 12.7 mm diameter steel tup (Fig. 2). Incident impact energies in the range 21–316 J were chosen by selecting the weight and the initial position of the impactor to obtain at least two tests with full penetration and another two tests without full penetration. The height of the tup was adjusted to obtain an impact velocity of ≈4 m/s in all cases to avoid strain rate effects and differences in the noise amplitude, which are proportional to the impact velocity [20]. The impactor was instrumented with a 50 kN load cell and an accelerometer to record continuously the applied force, P, and the tup displacement, d, and velocity.

Table 1
Characteristics of the composites.

Composite										
Short name	Commercial name	Supplier	Processing	Matrix	Fiber type	Tow cross-section (mm^2)	Porosity (%)	Fiber volume fraction	Thickness (mm)	Areal density (kg/m^2)
3D_S2	P3W-GS033/ Derakane 8084	3tex	Vacuum infusion	Epoxy vinylester	Warp 4 layers S2 glass 463-ΛΛ-250 Fill 5 layers S2 glass 463-AA-750	1.16	1.13	0.408	6.7	10.9
					DSK75 Dyneema uhmwe	0.4		0.079		
3D_C	P3W-D00001-hx21/ Derakane 8084	3tex	Vacuum infusion	Epoxy vinylester	Toray T300 carbon 100%	1.99	2.95	0.433	8.3	11.2
3D_hyb	P3W-D01-HX21/ Derakane 8084	3tex	Vacuum infusion	Epoxy vinylester	Agy S2-glass	1.18	11.6	0.275	4.1	6.3
					AS4C Carbon	0.931		0.141		
					Dyneema SK75 uhmwe	0.4		0.072		
2D_S2	6781/MTM44	ACG	Hot-press of prepreg	Epoxy	S2 glass 100%	0.032	4.2	0.507	4.1	7.5

Table 2
Characteristics of the dry fabrics.

Dry fabric								
Short name	Fabric architecture	Layers	Fiber type	Weight fraction (fabric)	TEX (g/km)	Nominal fiber Ø (µm)	Fabric thickness (mm)	Areal density (kg/m^2)
3D_S2	3D orthogonal woven	Warp 4 layers	S2 glass 463-AA-250	44.4	2033	9	7.34	7.29
		Fill 5 layers	S2 glass 463-AA-750	48.5	677	9		
		Through-thickness	Dyneema SK75 uhmwe	7.1	414	12–21		
3D_C	3D orthogonal woven	Warp 3 layers	Toray T300 12 k carbon	39	805.9	6.9	8.05	7.22
		Fill 4 layers	Toray T300 12 k carbon	52	805.9	6.9		
		Through-thickness	Toray T300 12 k carbon	9	805.9	6.9		
3D_hyb	3D orthogonal woven	4.5 layers	Agy S2-glass	72.3	1981	9	3.02	4.24
		2.5 layers	AS4C carbon	25.9	1607	6.9		
		Through-thickness	Dyneema SK75 uhmwe	1.8	414	12–21		
2D_S2	8-Harness satin weave	[(±45/0/90)2/0]$_s$	S2 glass	100	68	9	0.24/layer	0.302/layer

2.3. Damage characterization

Damage in the impacted specimens was studied by means of ultrasound and XCT. C-scans were performed on a TecniTest instrument. The backside (non-impacted) surface of the plates was scanned at 30 mm/s using a Sonatest SLG 5-102 transducer of 10 mm in diameter with a center frequency of 5 MHz. The interval between levels was 1 dB and the resolution was 1 mm. The commercial software Visual Scan V-1.0 was used to visualize the results. It should be noted that C-scan provides a damage envelop through the thickness of the plate but it does not offer information about the location of damage in the thickness direction nor about the type of damage. In addition, the color scale of the C-scans is relative and depends on the thickness of the specimen and the nature of the defects.

XCT was used to obtain detailed information about the actual damage mechanisms and their location through the thickness. The tomograms were performed with a Nanotom 160NF from Phoenix at 80–90 kV and 120–140 µA using either tungsten or molybdenum targets. 2000 radiographs were acquired for each tomogram with an exposure time of 750 ms. 3D tomograms were reconstructed from the radiographs using an algorithm based on the filtered back-projection procedure for Feldkamp cone beam geometry. The reconstructed volumes presented a resolution of 5–10 µm/voxel and were analyzed using the commercial package VGStudio Max. Emphasis was placed in the qualitative assessment of the main damage mechanism in each material as a function of the impact energy rather than in the quantification of specific damage modes (delaminated surface, volume of cracked tows, fraction of broken fibers, etc.).

3. Mechanical response under impact

A minimum of four impact tests were carried out on each material and impact energies were selected in such a way that full penetration was achieved in at least two specimens. Representative load–displacement (P–d) curves corresponding to three tests with different impact energies are shown in Fig. 3a–d for each material. They stand for one test in which full penetration was achieved, another test in which the tup was stopped before reaching the maximum load and an intermediate case.

The different P–d curves presented consistent results and the scatter was very limited. The mechanical response was initially smooth[1] and the impact energy was spent in the elastic deformation of the plate as well as in damage. This is demonstrated by the hysteresis in the unloading curves corresponding to the tests stopped

before the maximum load. Comparison of the of hysteresis loops corresponding to the 3D_S2 (Fig. 3a) and 2D_S2 (Fig. 3d) materials indicates that the 3D composite dissipated more energy due to damage in this regime, while elastic deformation with very little damage controlled the behavior of the 2D composite up to near to the maximum load.

High frequency oscillations in the load were observed in all P–d curves prior to the maximum load. They were caused by the brittle fracture of the fibers in tension in the backside surface of the plate as a result of bending. It should be noted that fracture of the glass fibers located in the backside occurred at a penetration of ≈14 mm in both the 3D_S2 and the 3D_hyb composites, while C fibers in the 3D_C material were broken when $d \approx 6$ mm. The 2D_S2 composite presented an intermediate behavior between both. After fiber fracture, the load carried by the plate decreased with the penetration depth until complete perforation was attained. Obviously, the tup displacement at perforation is very dependent on the plate thickness but comparison of Fig. 3c and d, corresponding to the 3D_hyb and 2D_S2 plates with the same thickness (4.1 mm) indicates that the 3D architecture was able to undergo larger deformations before perforation than the 2D laminate.

From the viewpoint of the impact resistance, the two critical parameters that define the composite behavior are the maximum load supported during impact and the energy absorbed. The latter is determined from the area under the P–d curve until full penetration is achieved (understood as the instant at which the load has dropped to $0.1 P_{max}$). As the materials studied have different areal densities (and weight minimization is an important design criterion in many composite applications), the maximum load and the energy dissipated normalized by the areal density are plotted in Fig. 4a and b, respectively, as a function of the plate thickness. The results for the 3D composites are shown as circles while those for the 2D laminates are plotted are squares. The figures also include previous results for 2D woven multidirectional composites reinforced with carbon fibers or a mixture of carbon and S2 glass fibers tested under the same conditions [15].

The normalized strength and energy dissipated by 2D_hyb and 2D_C composites were measured in plates with different thicknesses (in the range 5.5–7.5 mm) and they showed a mild increase with thickness (Fig. 4). From these results, it was concluded that S2 glass fiber 2D laminates were stronger and dissipated more energy under impact than carbon 2D laminates while hybrid 2D laminates were in between. In the case of the 3D composites, the carbon fiber composite showed lower normalized strength than the materials reinforced with glass S fibers but the normalized energy dissipated was equivalent in the three 3D materials. The differences in the behavior between the 3D_S2 and 3D_hyb composites were not conclusive, taking into account the differences in thickness in the plates of both materials.

---

[1] The ripples in the load–displacement curves corresponding to the 3D_C composite (Fig. 2b) are due to the reflection of the stress waves.
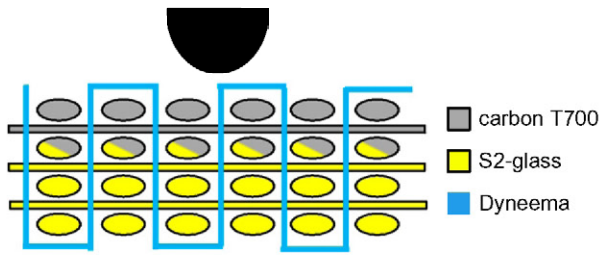
Fig. 1. Schematic of the cross-section of the 3D hybrid composite showing the fabric composition and architecture with respect to the tup position. (For interpretation of the references to color in this figure legend, the reader is referred to the web version of this article.)
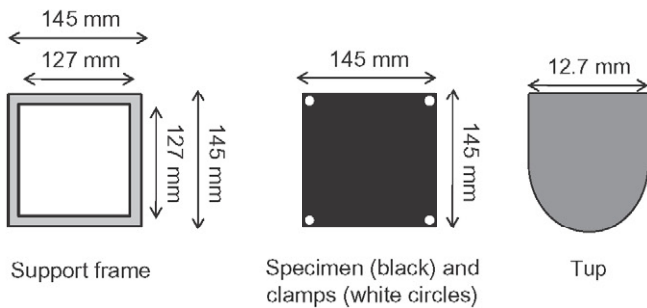

**Fig. 2.** Scheme of drop weight clamping system and tup geometries.

The higher load bearing capability of plates with S2 glass fibers in both 2D and 3D composites had been explained in the case of 2D composites by the higher strain-to-failure of the S2 glass fiber plies located near the top and bottom laminate surfaces [15]. These plies were able to sustain higher deformations before fracture and hindered the propagation of damage to the inner plies from the broken plies on the bottom and top surfaces, increasing the maximum load-bearing capability of the composite [15]. Regarding the effect of fiber type on the normalized energy dissipated during impact (Fig. 4b), the presence of S2 glass fibers clearly increased the energy dissipated in the 2D laminates and this was explained because they helped to sustain higher deformations before laminate fracture by the percolation of a through-thickness crack [15]. There are not, however, enough experimental data to draw definitive conclusions on the effect of fiber type on the energy absorption capability in 3D composites. By far, the most important factor controlling the impact response of the composite plates was the fiber architecture. Irrespective of the fiber type, tows characteristics, porosity degree and plate thickness, the normalized energy dissipated by 3D composites was – at least – twice higher than that spent by 2D laminates. Moreover, as abovementioned, the normalized maximum load of the 3D composites containing S2 glass fiber tows and PE z-yarns was the highest out of the composites under study. Thus, overall, the 3D composite containing S2 glass fibers for in-plane reinforcement and PE fibers for binders presented the best properties under low-velocity impact. Even larger differences between carbon and glass fiber composites are expected at
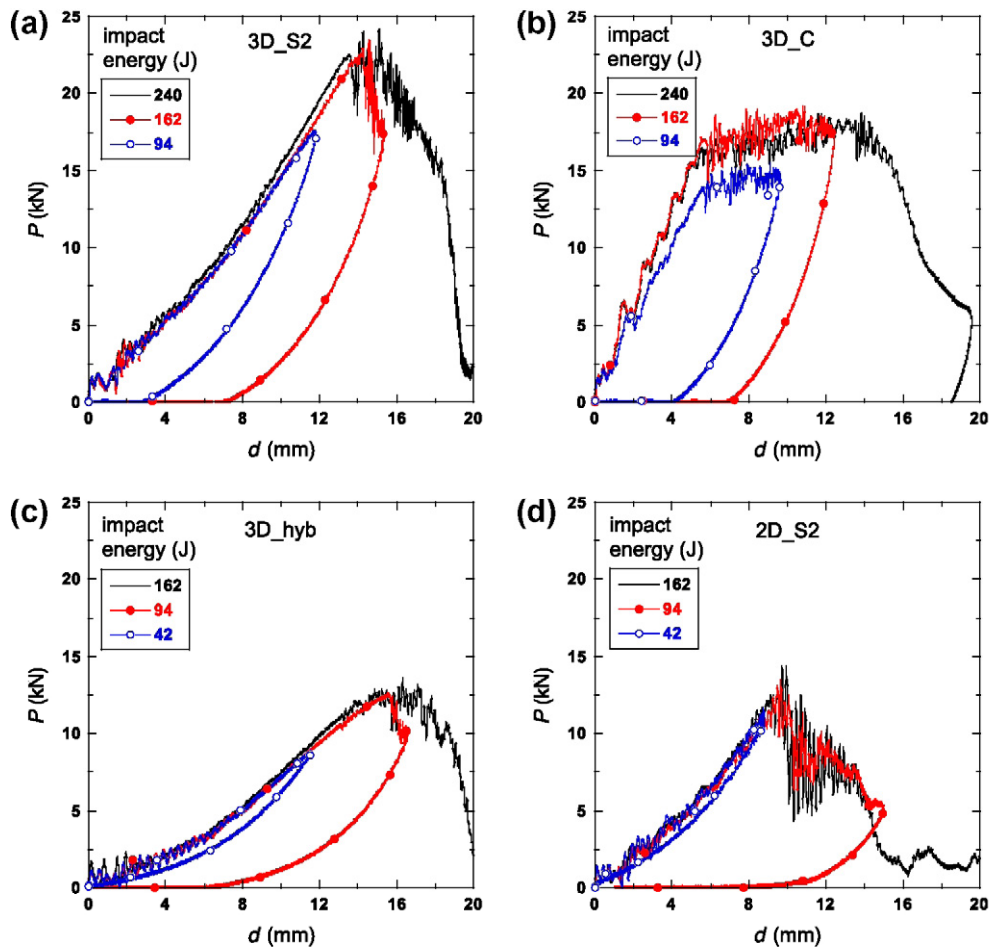
Fig. 3. Representative P–d curves from the low-velocity impact tests. (a) 3D_S2 composite. (b) 3D_C composite. (c) 3D_hyb composite. (d) 2D_S2 composite. (For interpretation of the references to color in this figure legend, the reader is referred to the web version of this article.)
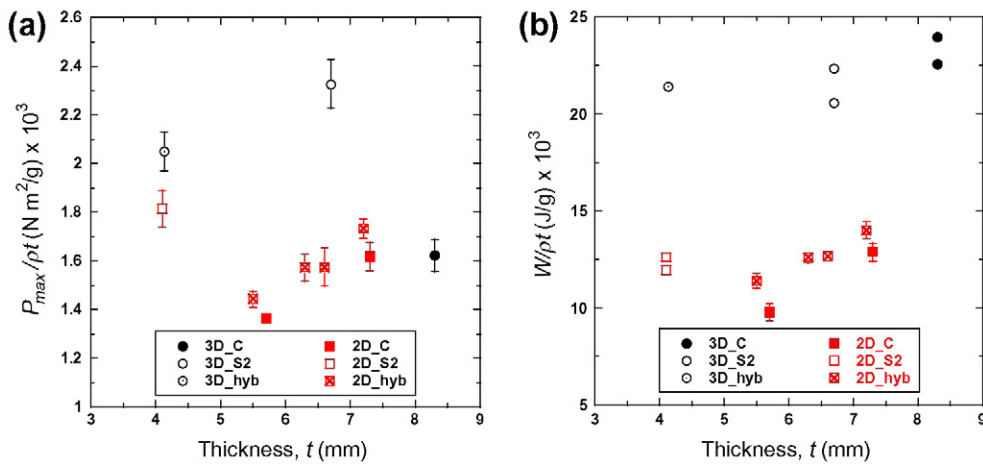
Fig. 4. (a) Maximum load, normalized by the areal density ρt, as a function of the laminate thickness, t. (b) Energy dissipated during impact, normalized by the areal density ρt, as a function of the laminate thickness, t. Data for 2D laminates with carbon fibers and hybrid S2/C reinforcements were taken from [15]. Error bars around the average values are provided if there were three or more experimental points. Otherwise, the actual results are plotted. (For interpretation of the references to color in this figure legend, the reader is referred to the web version of this article.)
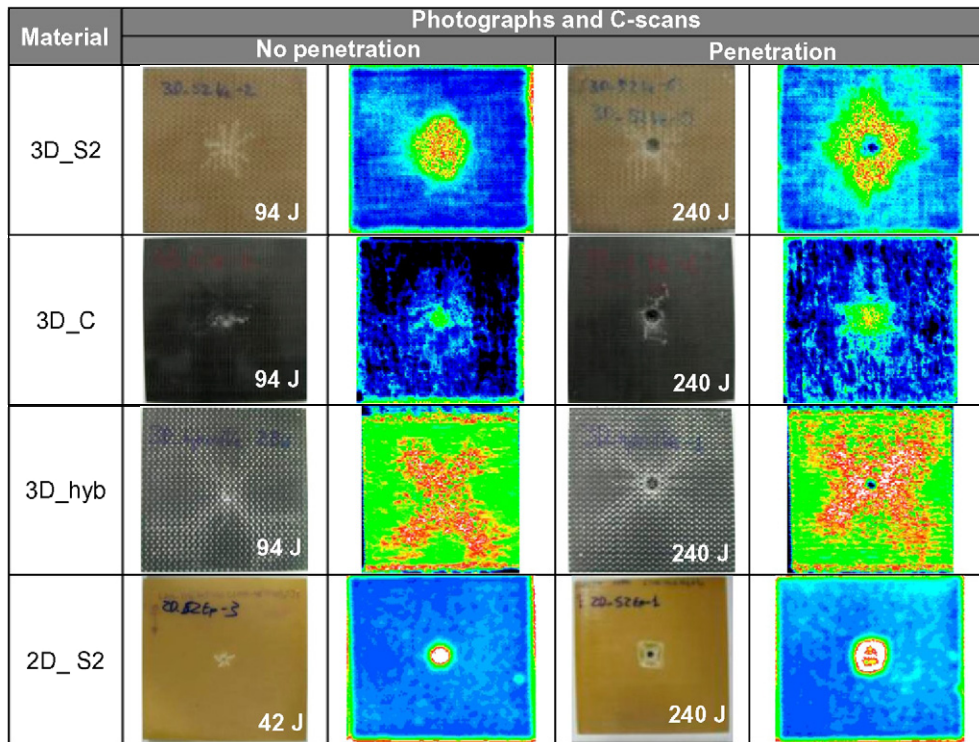
Fig. 5. Photographs of the back face and C-scans of the composite plates after impact. Results for two different impact energies are shown for each material, corresponding to no penetration and full penetration. The color scale is related to the depth of the first crack. The white-red regions stand for the cracks further away from the scanned surface, while undamaged regions are shown in black-navy blue. (For interpretation of the references to color in this figure legend, the reader is referred to the web version of this article.)

higher impact velocities since the apparent modulus and, particularly, the strength of glass fibers increase with strain rate.

The micromechanisms responsible for these results will be explored below.

4. Damage micromechanisms

4.1. Macroscopic damage patterns

The macroscopic damage patterns were assessed by means of ultrasound. The C-scans corresponding to two impact energies (one leading to full penetration and another in which the tup was stopped before full penetration) are shown in Fig. 5 for each material. The large differences in the energy dissipated by 3D and 2D composites are readily observed in this figure. Damage in the 2D laminate was localized around the impact point in the form a narrow ring with asymmetrical delaminated patches. Damage in the 3D composites emanated radially from the puncture site and was more spread. In addition, the C-scans of the 3D composites were speckled, contrasting with the relative continuity of colors in the 2D composite. This speckled appearance was indicative of discontinuous cracking but the particular features could only be ascertained by means of XCT.

At low impact energies, damage was spread evenly leaving a round damage envelope in all composites except in the 3D_hyb material, where diagonal directions were favoured. At high impact
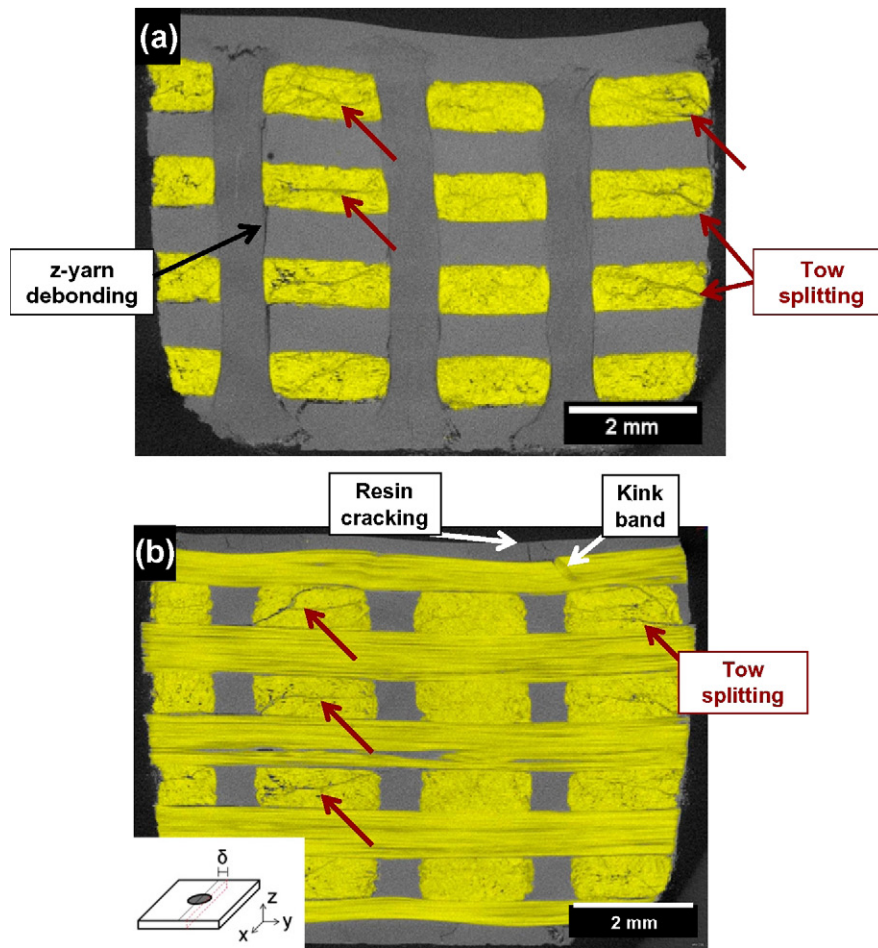
Fig. 6. Tomographic cross-sections (perpendicular to the *y* axis) of the 3D_S2 composite impacted with 94 J. (a) Cross-section below the impact center. (b) Cross section at δ = 1.7 mm from the impact center. PE z-yarns and resin are grey, while S2-glass fibers are yellow. Arrows with different colors indicate different failure micromechanisms. (For interpretation of the references to color in this figure legend, the reader is referred to the web version of this article.)

energies (leading to penetration), damage extended along the tow directions in all 3D composites, while the diagonal directions were also favoured in the 3D_hyb material. This was likely due to the influence of the boundary conditions on the deformation of the 3D_hyb plate, which was significantly thinner. Unlike the 3D composites, the perforated 2D composite plates presented a square damage envelope. This was due to fiber breakage of the outer-most layers with orientations +45° and −45° with respect to the specimen edges.

It is worth noting that damage in the 3D_C composite was more localized than in the 3D_S2 composite, although both materials had similar thickness. This can be attributed to the higher stiffness and brittleness of the carbon fibers. The 3D_hyb composite showed the largest damage extension and this can be explained in terms of the combination of the stiff carbon top layers that distributed the impact force on the bottom S2-glass fiber layers with higher capacity to deform in tension. It should be noted, however, that the extension of damage is also influenced by the fiber architecture and volume fraction and it is not the only parameter defining the energy absorption capability (Fig. 4b) because the energy spent in fiber fracture is order of magnitudes higher than that necessary for matrix cracking or delamination [14,21].

4.2. Damage micromechanisms

XCT was used to study the failure micromechanisms of the composites in closer detail. Two cross-sections of the 3D_S2 com-

posite impacted with 94 J are shown in Fig. 6 to elucidate the mechanisms of energy dissipation during the initial stages. Glass fiber tows are shown in yellow while the matrix and the PE z-yarns are grey. Fig. 6a corresponds to a cross-section just below the center of the impact in which the glass fiber tows perpendicular to the cross-section and the PE z-yarns are visible, while the glass fiber yarns perpendicular and parallel to the cross-section are shown in Fig. 6b, which was obtained at δ = 1.7 mm from the previous one. The main damage mechanism, indicated by red arrows in both micrographs, was the fracture of glass fiber tows by cracks parallel to the fibers (commonly denominated tow splitting). Most of these cracks were perpendicular to the impact direction and it is worth noting that practically no detectable cracks appeared immediately underneath the tup contact zone (the detection of cracks is limited to the current resolution of 5–10 μm/voxel). This indicated that the cracks were the result of shear and/or tensile stresses, rather than compressive stresses. Another interesting feature was that these intratow cracks did not propagate into the resin pockets. In addition, the PE z-yarns were debonded from the glass fiber tows and resin pockets due to the differences in elastic modulus (Fig. 6a). Finally, surface resin cracking and fiber kinking were also detected below the impact point (Fig. 6b).

The tomograms corresponding to the same composite impacted with 240 J are shown in Fig. 7. Fig. 7a and b shows cross-sections at the edge of the impact zone (5.9 and 5.5 mm, respectively). Glass fiber tows in the weft and warp directions are shown in Fig. 7a while the warp tows and the PE z-yarns are shown in Fig. 7b.
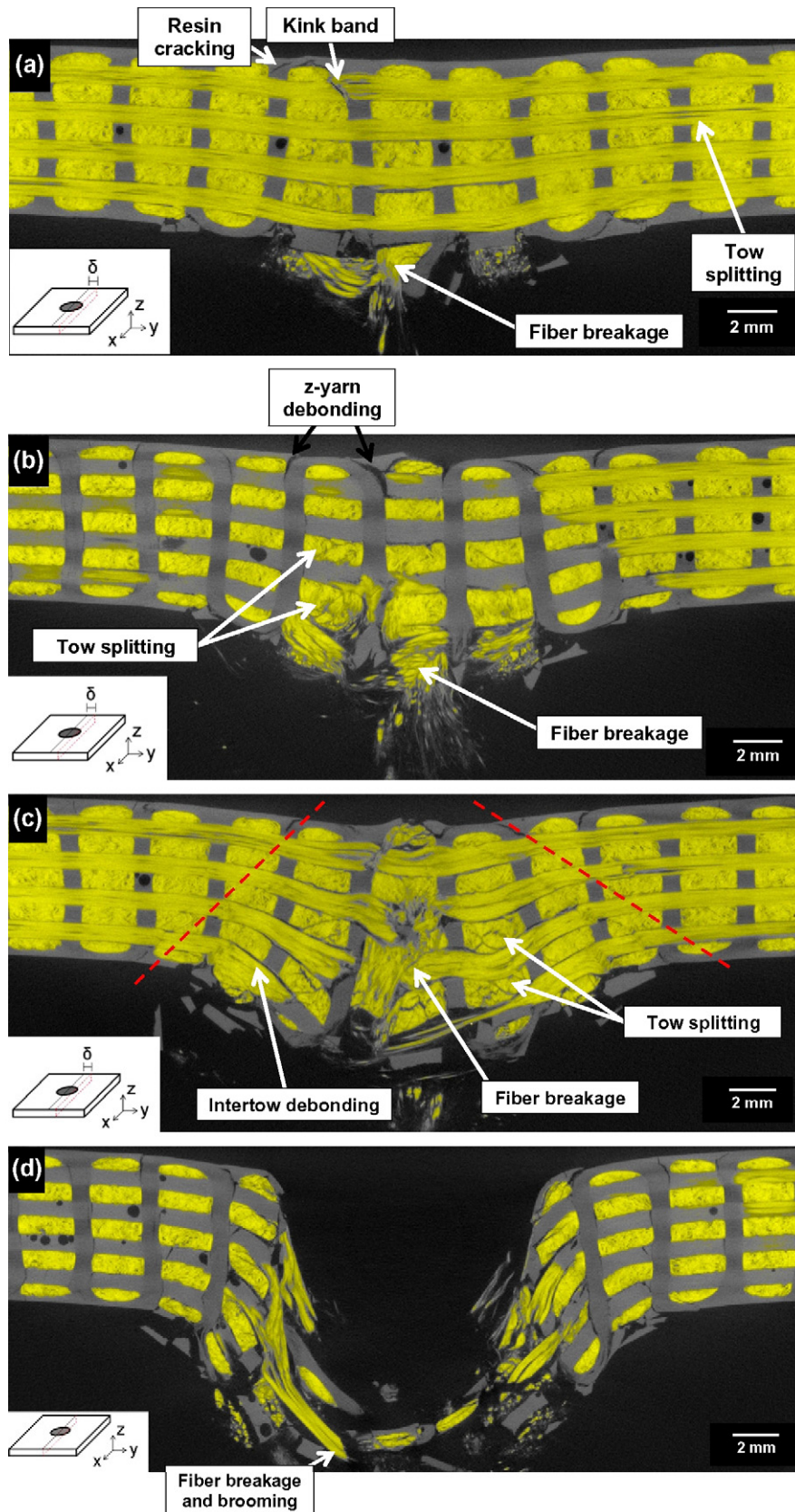
Fig. 7. Tomographic cross-sections (perpendicular to the *y* axis) of the 3D_S2 composite impacted with 240 J. (a) Cross section at δ = 5.9 mm from the impact center. (b) Cross section at δ = 5.5 mm from the impact center. (c) Cross section at δ = 4.2 mm from the impact center. (d) Cross-section below the impact center. PE z-yarns and resin are grey, while S2-glass fibers are yellow. Black regions are matrix voids. Arrows indicate different failure micromechanisms. (For interpretation of the references to color in this figure legend, the reader is referred to the web version of this article.)
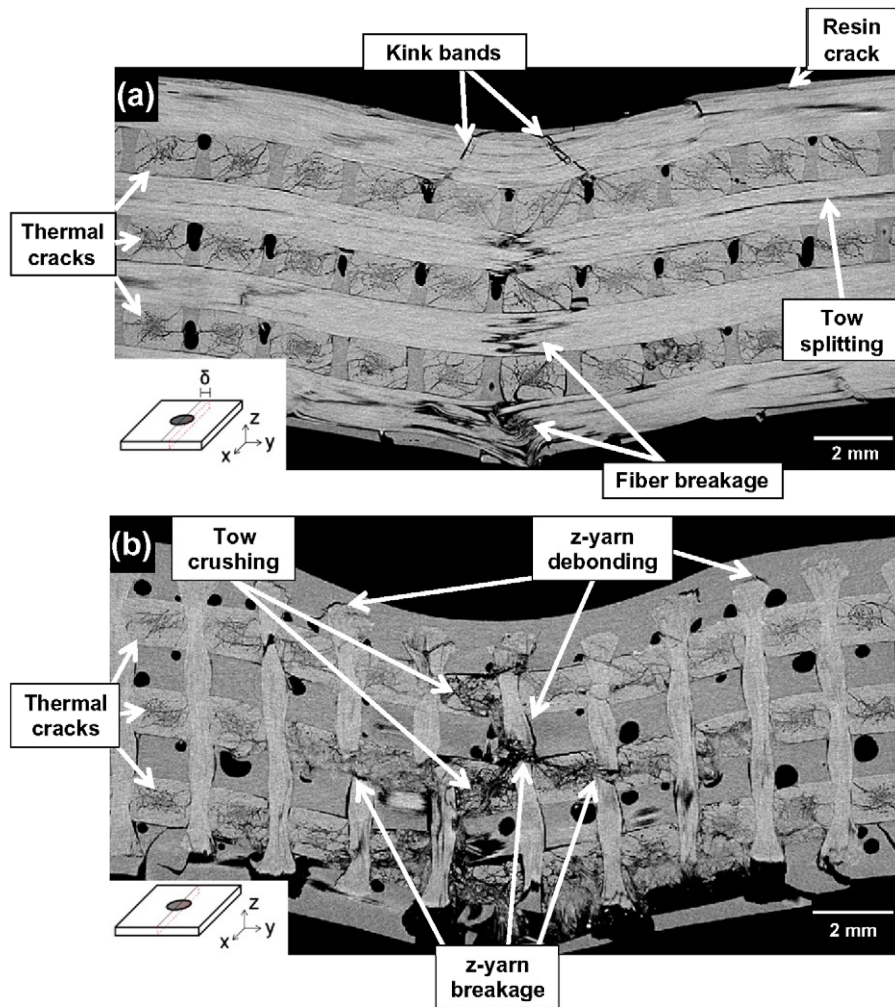
Fig. 8. Tomographic cross-sections (perpendicular to the *y* axis) of the 3D_C composite impacted with 94 J. (a) Cross section at δ = 3.2 mm from the impact center. (b) Cross section below the impact center. Carbon fibers (fiber tows and z-yarns) appear in light grey while the resin is grey. Black regions are matrix voids. Arrows indicate different failure micromechanisms. (For interpretation of the references to color in this figure legend, the reader is referred to the web version of this article.)

The damage mechanisms observed in Fig. 6, namely z-yarn debonding, surface resin cracking, fiber kinking and tow splitting are also seen (due to the lower resolution of these images, tow splitting in the glass fiber tows perpendicular to the cross section is difficult to appreciate). In addition, tensile fracture of the glass fibers is seen on the backside of the plate. It should be noticed that the whole 3D structure was held together by the PE z-yarns, which were able to deform without fracture. Closer to the impact center (Fig. 7c), tensile fracture of the weft and warp glass fiber tows has progressed from the backside towards the interior of the plate. PE z-yarns have started to fail in this highly-damaged region, leading to the development of intertow cracks (debonding). A fracture cone has developed emanating from the impact point (Fig. 7c). This cone is delimited by fiber microbuckling and tow bending, containing severe tow splitting within its boundaries. Just below the impact center, the tomograph (Fig. 7d) shows the formation of a plug under the tup in which the composite has completely failed surrounded by relatively intact material in which the 3D structure is held in place by the PE z-yarns. Thus, the penetration resistance of the plate predominantly depended on the out-of-plane shear strength, which seemed to be enhanced by the presence of the z-yarns.

The damage mechanisms of the 3D_C composite after impact with 94 J are shown in Fig. 8. The cross-section in Fig. 8a was obtained at 3.2 mm from the impact center and shows the warp and weft carbon fiber tows (light grey) together with the epoxy matrix (grey). Extended intratow cracking was present in this material throughout the cross-section due to the thermal residual stresses that develop upon cooling. Impact led to two main damage micromechanisms. carbon fiber tows were broken in the upper surface by fiber kinking due to the limited strain to failure of the C fibers. The kink bands propagated into the perpendicular carbon fiber tows but did not lead to detectable intertow delamination as the whole fabric was held together by the carbon z-yarns. In addition, tensile fiber fracture was observed in the carbon fiber tows located in the backside of the plate. Fiber fracture began at the bottom surface and progressed towards the center of the plate. Fig. 8b shows another cross-section of the same plate just below the impact point. In this cross-section, the carbon z-yarns (in light grey) are clearly identified. The z-yarns suffered extensive debonding from the matrix and the C fiber tows as well as z-yarn breakage. The carbon fiber tows presented tow splitting underneath the contact zone. This type of cracks are differentiated from the thermal cracks by their extension, branching and crack opening. It is worth noting that the PE z-yarns of the 3D_S2 composite were intact after impact with the same energy (Fig. 6a).

The cross-sections of the tomograms of the 3D_C composite impacted with 240 J are shown in Fig. 9. At the edge of the impact site
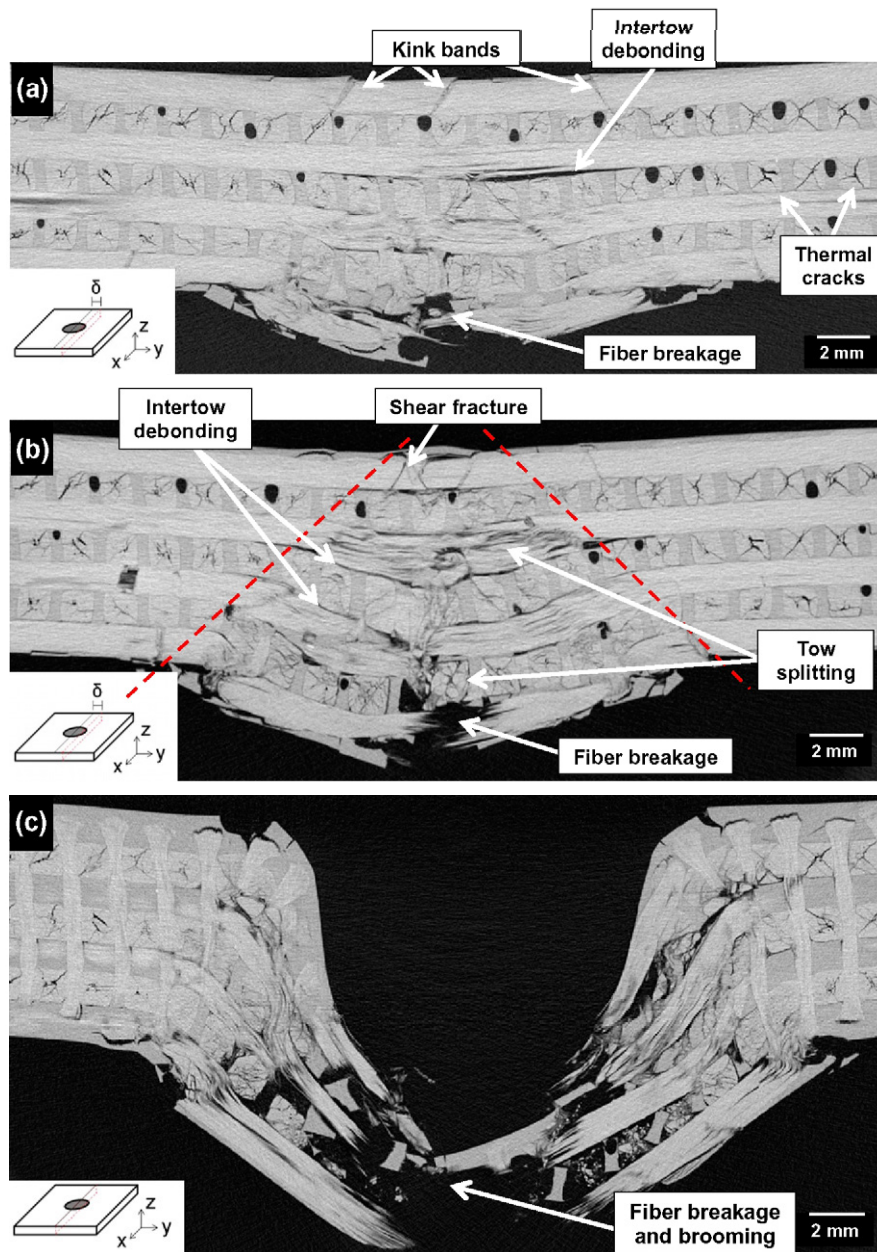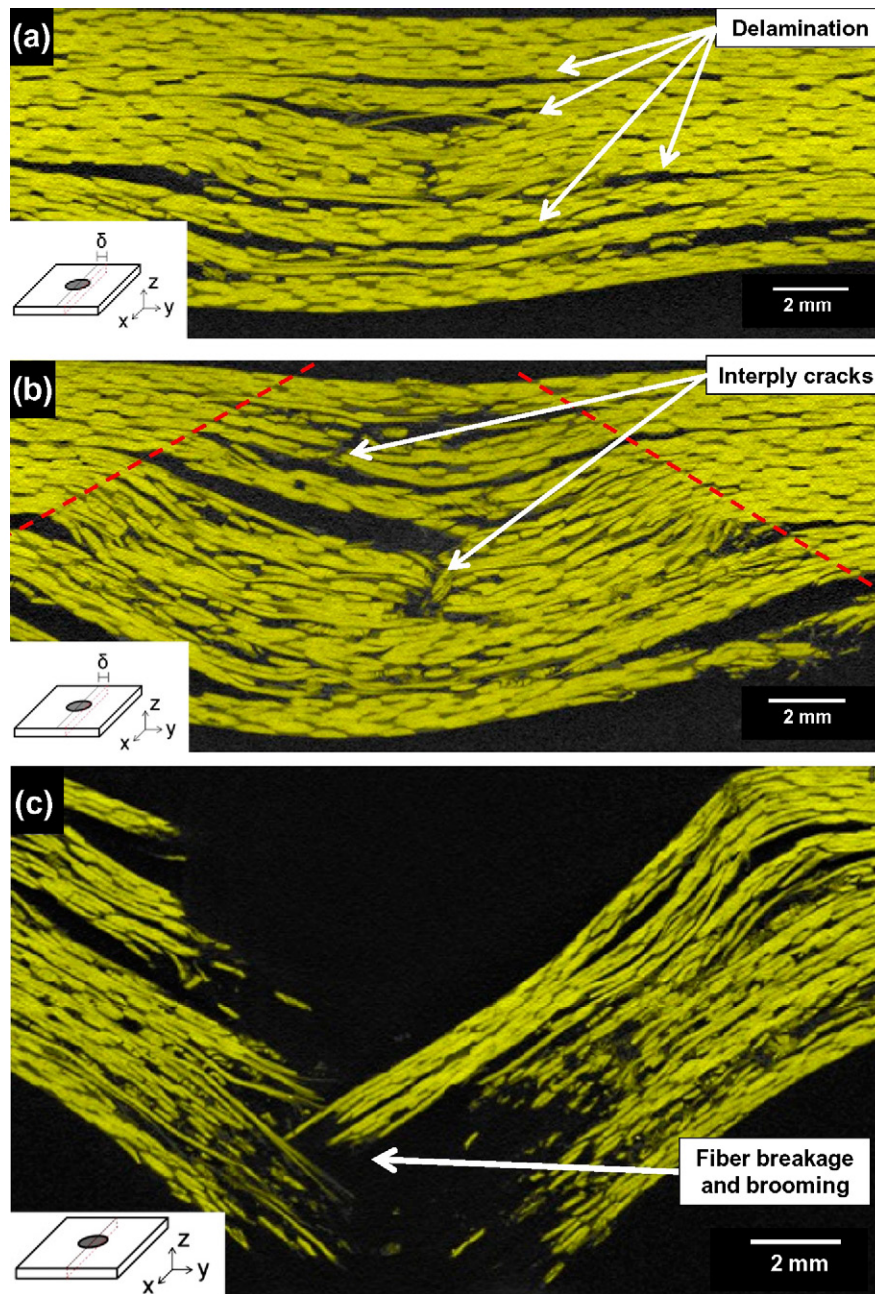
Fig. 9. Tomographic cross-sections (perpendicular to the y axis) of the 3D_C composite impacted with 240 J. (a) Cross section at δ = 7.6 mm from the impact center. (b) Cross section at δ = 6.2 mm from the impact center. (c) Cross-section below the impact center. carbon fibers (fiber tows and z-yarns) appear in light grey while the resin is grey. Arrows indicate different failure micromechanisms. (For interpretation of the references to color in this figure legend, the reader is referred to the web version of this article.)

(Fig. 9a), the main damage mechanisms observed are kink bands in the upper surface and fiber breakage in the backside surface. In addition, intertow debonding was initiated between warp and weft plies due to the fracture the carbon z-yarns. Fiber breakage in tension, fiber shear cracks and tow splitting were more noticeable closer to the impact center (Fig. 9b), leading to the formation of a fracture cone. As in the 3D_S2 composite, the cone is delimited by fiber microbuckling and tow bending. The cross-section of the fully-penetrated composite below the impact point is shown in Fig. 9c, showing again the formation of a plug of material under the tup in which damage was localized. This plug mainly developed by out-of-plane shear, as in the 3D_S2 composite.

Cross-sections of the tomograms obtained on the 3D_hyb composite provided similar results to those found in the 3D_S2 material and are not included for the sake of brevity. Damage began

by formation of shear cracks in the upper carbon fiber layers, followed by tensile fracture of glass fibers in the bottom layers. The whole 3D fabric was maintained in place by the PE z-yarns except below the impact center in the tests at high impact energy. Summarizing, despite the differences in plate thickness, fiber type, yarns characteristics, compaction and porosity degree, the three 3D orthogonal woven composites presented these common stages before perforation occurred: deep indentation of the plate, formation of a plug below the tup, and, ultimately, highly localized fiber breakage in tension.

These damage mechanisms are rather different from those reported in 2D woven composites [9,15,21–23]. To illustrate these differences, various cross-sections of the 2D_S2 laminate impacted with 240 J are shown in Fig. 10. The first damage mechanism observed in the cross-section was interply delamination (Fig. 10a). It is very likely that tow splitting also occurred in the upper surface

Fig. 10. Tomographic cross-sections (perpendicular to the *y* axis) of the 2D_S2 laminate impacted with 240 J. (a) Cross section at δ = 7.8 mm from the impact center. (b) Cross section at δ = 5.8 mm from the impact center. (c) Cross-section below the impact center. Glass fibers appear in yellow. Arrows indicate different damage mechanisms. (For interpretation of the references to color in this figure legend, the reader is referred to the web version of this article.)

but it could not be clearly observed with the resolution of these tomograms. In absence of the constraint imposed by the z-yarns, delamination cracks grew rapidly (Fig. 10b) and eventually deflected into the lower or upper ply by matrix shear cracking due to the presence of large shear stresses radiating from the contact point in a conical fashion. This process was repeated several times, leading to a conical damage zone starting from the contact point and circumscribed by bended tows. Fiber microbuckling, as in the case of the 3D composites, was not identifiable. The damage inside the cone is composed of transverse matrix cracks and interply delaminations (Fig. 10b). Final fracture below the impact point was triggered by tensile fiber failure, as shown in Fig. 10c, leading to fiber brooming, a combination of tow longitudinal splitting, fiber breakage, fiber pull-out and disentanglement. As opposed to the

3D composites, out-of-plane shear was not the main mechanism leading to penetration in this material of this material.

5. Discussion

The results of the low-velocity impact tests demonstrated that the energy absorption capability of the 3D composites was significantly enhanced over those of the 2D laminates. This difference correlates well with the results of ultrasound inspections of the impacted plates, which showed that the extent of the damaged zone was higher in the former, but – to the authors' knowledge – no detailed investigation of the micromechanisms of damage in 3D composites was available. This information was obtained by means of

XCT and will be discussed here to ascertain the energy dissipation mechanisms before the maximum load and the factors controlling the impact strength and the total energy dissipated during penetration.

In the case of the 2D laminates, damage began by interply delamination (see also [15]). These interply cracks spread and diverted into other plies, leading to further delamination, which is the main energy dissipation mechanism in 2D laminates prior to attain the maximum load (Fig. 10a). Detectable interply delamination was, however, impeded in the case of the 3D composites by the confining effect of the z-yarns. As a result, energy dissipation by tow splitting within the fiber yarns was spread through the thickness of the cross-section. Furthermore, the open architecture of the 3D fabrics led to the promotion of fiber fracture by kinking and shear which dissipate a larger amount of energy [21]. These mechanisms – together with minor contributions from resin cracking and debonding of the z-yarns – were responsible for the higher energy dissipation in the 3D composite during the initial stages of the impact.

The maximum load borne by the 2D and 3D composites upon low-velocity impact was determined by the onset of tensile fiber fracture in the backside surface. This was controlled by the overall stiffness of the plate and by the strain-to-failure of the fibers, being the composites with any amount of S2 glass fiber generally stronger than the composites with solely carbon fibers. After reaching maximum load, the load born by the composite decreased with the tup displacement until complete perforation. Most of the impact energy was absorbed in this regime and the mechanisms contributing to energy dissipation in the 2D laminates were fiber fracture and interply delamination, irrespective of their fiber type. They were localized in a conical volume initiated at the impact point and the major contribution to energy dissipation was provided by fiber fracture, as interply toughness is low (Fig. 10b and c). In the case of the 3D composites, damage was also localized in a cone (Figs. 7c and 9b) but it was accompanied by deep penetration of the tup into the material and plug formation by severe out-of-plane shear (Figs. 7d and 9c). This enhanced the energy dissipation by extensive tow splitting and fiber breakage in compression and shear under the tup. All these mechanisms increased dramatically the energy dissipated during impact and were responsible for the results in Fig. 4b, where 3D composites absorbed, approximately, twice more energy than 2D laminates. Composites reinforced with S2 glass fibers presented larger deformability as compared with C fibers and this factor also contributed to the energy dissipated in this regime.

Finally, the current experimental observations do not allow a definitive conclusion on the influence of the type of z-yarns (either PE or carbon) on the performance of 3D composites, although marked differences in the mechanical behavior of PE and carbon z-yarns were found. While the carbon z-yarns presented early failure during impact, PE fibers failed after significant deformation. Thus, PE z-yarns performed better than carbon z-yarns in order to maintain longer the integrity of the 3D composites below the tup.

6. Conclusions

The damage micromechanisms in 3D woven composites under low-velocity impact were studied by means of X-ray microtomography. 2D composites with the best suited architecture to resist out-of-plane loading, i.e. 2D woven multidirectional laminates, were also analyzed for comparison, leading to the following conclusions:

- The 3D fiber architecture enhanced the energy dissipated during low-velocity impact by a factor of ≈2, as compared with 2D laminates, regardless of the type of reinforcement. The z-yarns maintained the structural integrity of the laminate and

promoted deep indentation of the tup, and thus, intensive energy dissipation by tow splitting, fiber breakage, and formation of a plug by out-of-plane shear.The maximum load borne by the composite under low-velocity impact was controlled by the onset of tensile fiber fracture at the backside surface. Thus, the main factor controlling the maximum load was the in-plane fiber type, with S2 glass fibers performing better than carbon fibers.

- Out of the composites studied in the present work, the 3D orthogonal woven composites with S2 glass fibers for in-plane reinforcement and PE fibers for binders presented the best properties in terms of maximum load and energy dissipation (normalized by the areal density) under low-velocity impact.

References

[1] Schoeppner GA, Abrate S. Delamination threshold loads for low velocity impact on composite laminates. Composites: Part A 2000;31:903–15.
[2] Cox BN, Dadkhah MS, Morris WL, Flintoff JG. Failure mechanisms of 3D woven composites in tension, compression, and bending. Acta Metall Mater 1994;42(12):3967–84.
[3] Cox BN, Dadkhah MS, Morris WL. On the tensile failure of 3D woven composites. Compos Part A: Appl Sci Manuf 1996;27(6):447–58.
[4] Ko FK, Hartman D. Impact behavior of 2-D and 3-D glass/epoxy composites. SAMPE J 1986;22(4):26–30.
[5] Ansar M, Xinwei W, Chouwei Z. Modeling strategies of 3D woven composites: a review. Compos Struct 2011;93(8):1947–63.
[6] LLorca J, González C, Molina-Aldareguía JM, Segurado J, Seltzer R, Sket F, et al. Multiscale modeling of composite materials a roadmap towards virtual testing. Adv Mater 2011;23:5130–47.
[7] Walter TR, Subhash G, Sankar BV, Yen CF. Damage modes in 3D glass fiber epoxy woven composites under high rate of impact loading. Compos Part B: Eng 2009;40(6):584–9.
[8] Baucom JN, Zikry MA. Evolution of failure mechanisms in 2D and 3D woven composite systems under quasi-static perforation. J Compos Mater 2003;37(18):1651–74.
[9] Baucom JN, Zikry MA, Rajendran AM. Low-velocity impact damage accumulation in woven S2-glass composite systems. Compos Sci Technol 2006;66(10):1229–38.
[10] Schilling PJ, Karedla BPR, Tatiparthi AK, Verges MA, Herrington PD. X-ray computed microtomography of internal damage in fiber reinforced polymer matrix composites. Compos Sci Technol 2005;65(14):2071–8.
[11] Wright P, Moffat A, Sinclair I, Spearing SM. High resolution tomographic imaging and modelling of notch tip damage in a laminated composite. Compos Sci Technol 2010;70(10):1444–52.
[12] Awaja F, Nguyen M, Zhang S, Arhatari B. The investigation of inner structural damage of UV and heat degraded polymer composites using X-ray micro CT. Compos Part A: Appl Sci Manuf 2011;42(4):408–18.
[13] Hernández S, Sket F, Molina-Aldareguía JM, González C, LLorca J. Effect of curing cycle on void distribution and interlaminar shear strength in polymer–matrix composites. Compos Sci Technol 2011;71:1331–41.
[14] Sket F, Seltzer R, Molina-Aldareguía JM, González C, LLorca J. Determination of damage micromechanisms and fracture resistance of glass fiber/epoxy cross-ply laminate by means of X-ray computed microtomography. Compos Sci Technol 2012;72:350–9.
[15] Enfedaque A, Molina-Aldareguía JM, Gálvez F, González C, Llorca J. Effect of glass fiber hybridization on the behavior under impact of woven carbon fiber/epoxy laminates. J Compos Mater 2010;44(25):3051–68.
[16] Mahadik Y, Hallett SR. Effect of fabric compaction and yarn waviness on 3D woven composite compressive properties. Compos Part A: Appl Sci Manuf 2011;42(11):1592–600.
[17] Gerlach R, Siviour CR, Wiegand J, Petrinic N. In-plane and through-thickness properties, failure modes, damage and delamination in 3D woven carbon fibre composites subjected to impact loading. Compos Sci Technol 2012;72(3):397–411.
[18] Evci C, Gülgeç M. An experimental investigation on the impact response of composite materials. Int J Impact Eng 2012;43:40–51.

[19] David-West OS, Alexander NV, Nash DH, Banks WM. Energy absorption and bending stiffness in CFRP laminates: the effect of 45° plies. Thin-Walled Struct 2008;46(7–9):860–9.

[20] Found MS, Howard IC, Paran AP. Interpretation of signals from dropweight impact tests. Compos Struct 1998;42(4):353–63.

[21] Lopes CS, Camanho PP, Gürdal Z, Maimí P, González EV. Low-velocity impact damage on dispersed stacking sequence laminates. Part II: Numerical simulations. Compos Sci Technol 2009;69(7–8):937–47.

[22] Davies GAO, Hitchings D, Zhou G. Impact damage and residual strengths of woven fabric glass/polyester laminates. Compos Part A: Appl Sci Manuf 1996;27(12):1147–56.

[23] Schoeppner GA, Abrate S. Delamination threshold loads for low velocity impact on composite laminates. Compos Part A: Appl Sci Manuf 2000;31(9): 903–15.